COMMUNICATION

Check for updates
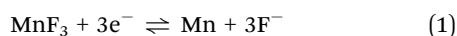
Manganese electrode for all-solid-state fluoride batteries†

Atsushi Inoishi, [iD] *[ab] Naoko Setoguchi,[a] Megumi Motoyama,[a] Shigeto Okada[b] and Hikari Sakaebe [iD] [ab]

We investigate MnF$_3$ as an electrode material for all-solid-state fluoride batteries. The initial discharge capacity due to defluorination was 535 mA h g^{-1}. Manganese was confirmed to be reduced and oxidized during charge–discharge measurements. Metallic Mn was also reversibly fluorinated and defluorinated as a starting material.

Fluoride batteries have attracted attention as next-generation batteries because of their high chemical stability and high theoretical energy density due to the flexible choice of electrode materials. Fluoride (F$^-$) anions function as charge carriers in fluoride batteries; therefore, various metals are potential candidates for the conversion-type electrodes.[1] In addition, there is a wide variety of solid electrolytes, including PbSnF$_4$, BaSnF$_4$, BaCaF$_4$, and tysonite-type and BaF$_2$-based fluorites.[1–16] In 2011, A. Reddy *et al.* reported the first all-solid-state fluoride battery, and since then, there have been many recent reports of all-solid-state fluoride batteries.[17–32] We recently reported the application of a FeF$_3$ cathode for fluoride batteries, where a large discharge capacity of 579 mA h g^{-1} was observed at first discharge.[29] In addition, many groups reported CuF$_2$ as a cathode material for fluoride batteries.[18,27] As such, transition metal fluorides have been shown to be promising cathode materials for large-capacity batteries. Among the possible electrode materials for fluoride batteries, MnF$_3$ has advantages of a large theoretical capacity (718 mA h g^{-1}) and low cost. The theoretical gravimetric energy density for a full cell composed of a MnF$_3$ cathode and a Mg anode is 1127 W h kg^{-1}, which is comparable with that for a FeF$_3$ cathode. However, in the case of Li$^+$-ion batteries, manganese fluoride shows a large overpotential.[28] On the other hand, the following simple reaction may occur in the fluoride battery:

$$MnF_3 + 3e^- \rightleftharpoons Mn + 3F^- \qquad (1)$$

^{a} *Institute for Materials Chemistry and Engineering, Kyushu University, 6-1 Kasuga-koen, Kasuga 816-8580, Japan. E-mail: inoishi@cm.kyushu-u.ac.jp*

^{b} *Transdisciplinary Research and Education Center for Green Technology, Kyushu University, 6-1 Kasuga-koen, Kasuga-Shi 816-8580, Japan*

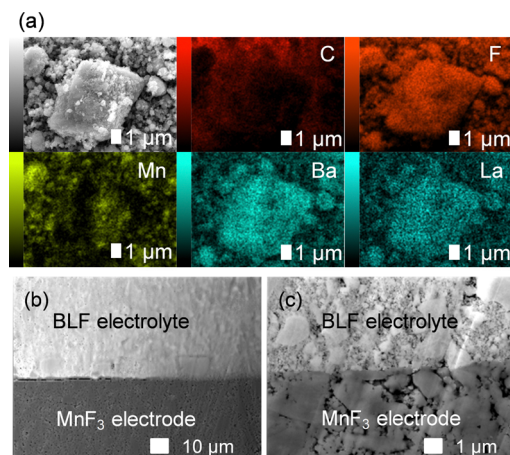† Electronic supplementary information (ESI) available. See DOI: https://doi.org/10.1039/d4cc04418e

This reaction does not form the LiF insulator, which is typically formed in lithium-conversion type batteries when metal fluorides are used as an electrode material. Therefore, the use of MnF$_3$ as an electrode in fluoride batteries is considered to be reasonable with respect to advantages such as the low cost and large capacity. Here we report all-solid-state fluoride batteries based on a MnF$_3$ electrode with Ba$_{0.6}$La$_{0.4}$F$_{2.4}$ (BLF) used as the electrolyte and a Pb-based counter electrode.

Fig. S1 (ESI†) show SEM images of the MnF$_3$ powder before and after ball-milling. Although the particle size before ball-milling was 100 nm–3 μm, that after mechanical ball-milling at 600 rpm for 12 h was more uniform at 100 nm–1 μm. The crystallinity of the MnF$_3$ powder was significantly decreased after ball-milling (Fig. S2, ESI†). The electrochemical performance was evaluated at 433 K because of the large IR drop in the solid BLF electrolyte at room temperature. Considering high-temperature operation, the chemical stability of MnF$_3$ was evaluated at high temperatures. XRD patterns for MnF$_3$ after heating at various temperatures under Ar are shown in Fig. S3 (ESI†). Peaks assigned to MnF$_3$ were observed up to 433 K; however, MnF$_3$ was decomposed at 473 K and peaks assigned to MnF$_2$ were newly formed. On the other hand, FeF$_3$ is stable even at 473 K, as we previously reported.[29] Therefore, FeF$_3$ is more stable than MnF$_3$ at high temperature. Fig. 1(a) shows SEM images of the MnF$_3$-based composite powder (MnF$_3$, BLF, acetylene black(AB)). The primary BLF solid electrolyte particles were smaller than 1 μm and secondary particles were larger than 10 μm, which is good agreement with our previous study.[29] Fig. 1(b) and (c) show cross-sectional images of the BLF/MnF$_3$ electrode interface after heating at 433 K. Fig. 1(b) shows both a highly connected interface region and a region where separation has occurred. Fig. S4 (ESI†) shows a cross-sectional SEM image of the MnF$_3$ electrode/BLF electrolyte interface after heating at 433 K. The thickness of the MnF$_3$ electrode was 88 μm. Fig. 2(a) shows discharge–charge curves for an all-solid-state fluoride battery with a Pb/PbF$_2$–SnF$_2$–AB/BLF/MnF$_3$–BLF–AB structure between −2 V and 2 V at 433 K

Fig. 1 SEM images of MnF$_3$-based composite electrode and electrode/electrolyte interface for fluoride battery cell. (a) SEM image and energy dispersive spectroscopy (EDS) elemental maps of as-synthesized electrode powder. (b) and (c) Cross sectional images of BLF/MnF$_3$ electrode interface after heating at 433 K (1000× and 10 000× magnification).

(defluorination of MnF$_3$). The initial discharge capacity (starting from defluorination) was 535 mA h g^{-1}, which was 75% of the theoretical capacity for MnF$_3$ (718 mA h g^{-1}). Therefore, 2.2 F$^-$ ions were shuttled from the MnF$_3$ electrode during the initial discharge. This indicates that most of the MnF$_3$ is decomposed to MnF$_2$ before discharge. The observed capacity is larger than that reported for BiF$_3$ or CuF$_2$ electrodes at 413 K in an all-solid-state fluoride battery.[17,27] However, this is still lower than that for an FeF$_3$ electrode (579 mA h g^{-1} at first cycle), which was reported in our previous study.[29] The observed single potential plateau is in good agreement with the theoretical redox potential for MnF$_2$/Mn (−0.991 vs. PbF$_2$/Pb) and also

Fig. 2 Charge−discharge profiles for all-solid-state fluoride battery with MnF$_3$ electrode in ranges of (a) −2 V to 2 V, and (b) −2 V to 4 V (starting from defluorination of MnF$_3$). Cell structure is Pb/PbF$_2$−SnF$_2$−AB/BLF/MnF$_3$−BLF−AB. The capacity was calculated based on the weight of MnF$_3$.

indicates that the initial state before discharge is mainly MnF$_2$. A discharge capacity of 290 mA h g^{-1} was retained at the 50th cycle. The open-circuit voltage gradually increased with cycling, which indicates that the oxidation state of manganese is gradually increased, but is mainly charged to the Mn^{2+} state. Fig. 2(b) shows discharge–charge curves for the all-solid-state fluoride battery with a MnF$_3$ electrode in the range of −2 V to 4 V at 433 K (starting from defluorination). The cell structure is the same as that in Fig. 2(a). Unlike the case for −2 V to 2 V (Fig. 2(a)), a discharge plateau is observed between 0 and 1 V and a charge plateau between 1 and 3 V. The theoretical potentials for the MnF$_3$/MnF$_2$ and MnF$_2$/Mn couples are 1.217 V (vs. PbF$_2$/Pb) and −0.991 V (vs. PbF$_2$/Pb), respectively. The observed potential plateaus are reasonably matched with these theoretical potentials, as shown in Fig. S5 (ESI†), which indicates that manganese is reduced and oxidized. By comparison with Fig. 2(a), oxidation of Mn^{3+}/Mn^{2+} should occur between 1 V and 2 V, and also above 2 V. The potential and capacity of the Mn^{3+}/Mn^{2+} region gradually increased with cycling, which may be due to stabilization of the Mn^{3+} species. The discharge capacity of 489 mA h g^{-1} at the 10th cycle is larger than that for FeF$_3$ (461 mA h g^{-1} at the 10th cycle) within the same potential range.[29] On the other hand, the hysteresis of the discharge–charge curve was dependent on the voltage range. The voltage difference for the 10th discharge–charge cycle at 350 mA h g^{-1} (see the point in Fig. S6, ESI†) is 0.945 V between −2 V and 2 V and 0.641 V between −2 V and 4 V. The decrease in overpotential after charging to 4 V may be related to the formation of Mn^{3+} species; however, this has yet to be verified. On the other hand, the voltage difference for the 10th discharge–charge cycle at 350 mA h g^{-1} for the FeF$_3$ and MnF$_3$ electrodes are 0.753 V and 0.641 V, respectively. Therefore, the overpotential of the MnF$_3$ electrode is much lower than that of the FeF$_3$ electrode when the voltage range of the charge–discharge measurement is between −2 V and 4 V. The IR drop for the BLF solid electrolyte is 0.06 V during operation (433 K and 80 μA cm^{-2}); therefore, the internal resistance between 2 V and 4 V, excluding the IR drop, is 0.58 V. This is much lower than that for a manganese fluoride electrode for a lithium battery.[33] These results suggest that the charge transfer resistance differs significantly depending on the discharge–charge mechanism, although the operating temperature is different. In the case of lithium battery, insulating LiF is formed during conversion reaction. The effect of operating temperature on the all-solid-state fluoride battery with a MnF$_3$ electrode was investigated (Fig. S7, ESI†). The cell was heated once to 433 K, then cooled to each respective temperature for measurement (413 K and 393 K). The initial defluorination capacities at 413 K and 393 K were 215 mAhg^{-1} defluorination capacities at 413 K and 393 K were 215 mA h g^{-1} and 41 mA h g^{-1}, respectively, showing a substantial decrease compared to the performance at 433 K. A significant factor contributing to this high resistance is the decreased ionic conductivity of the electrolyte, indicating that applying a solid electrolyte with high conductivity at lower temperatures is essential for reducing the operating temperature. Ex situ XAS measurements were conducted to clarify the
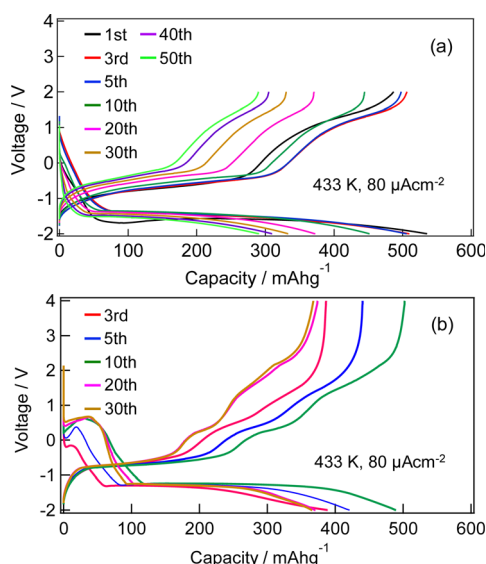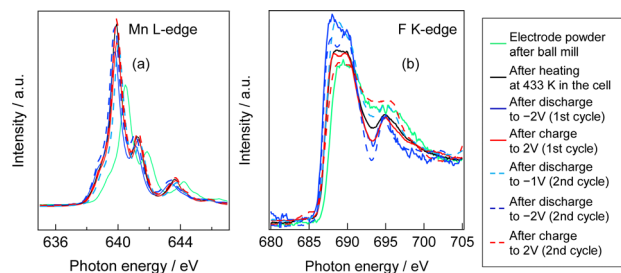
Fig. 3 (a) Mn L-edge and (b) F K-edge XAS spectra of MnF_3 electrode obtained from current collector side.

discharge–charge mechanism for the MnF_3 electrode. Fig. 3(a) and (b) show Mn L-edge and F K-edge X-ray adsorption spectra of the MnF_3 electrode before and after the discharge–charge measurements. Peaks associated with L3 and L2 can be observed in this region of the Mn L-edge spectra.[34] Following heating of the constructed cell, the XAS peak positions shifted to lower energy. This indicates that MnF_3 is decomposed or reacts with the BLF electrolyte or AB in the composite electrode due to the high temperature or high pressure during construction of the cell. Therefore, the MnF_3 composite electrode is not sufficiently stable in this structure. The adsorption peak at around 640 eV associated with MnF_3 decreased after discharging and was then recovered after charging. Therefore, the Mn-based species is active for the redox reaction. As shown in Fig. S8 (ESI†), The F K-edge XAS spectra for the MnF_3 electrode charged at different voltages (yielding MnF_3 and MnF_2) revealed the formation of Mn^{3+} by the peak at around 684 V observed after charging to 4 V, which is in contrast to the electrode charged to 2 V (no adsorption due to MnF_2 was observed around this region, Fig. S8, ESI†), i.e., Mn^{3+} is formed only after charging to 4 V. We have reported that the BLF of the solid electrolyte shows two peaks around 689 eV in our previous work.[29] In the charged state of manganese fluoride electrode (Fig. 3(b)), contributions from the fluorine in manganese fluoride overlap, so clearly split peaks assigned to BLF electrolyte are not observed. On the other hand, after discharge in the second cycle, the spectrum is very similar to that of BLF, suggesting that metallic Mn is formed. From these results, the changes in the F K-edge spectrum indicate that a reversible redox reaction is occurring between manganese fluoride and metallic manganese. The XRD pattern after charging to 2 V did not indicate any formation of manganese fluoride; the species formed was thus amorphous (Fig. S9, ESI†). Fig. S10 (ESI†) shows SEM images of the MnF_3 electrode before and after 58 cycles between −2 V and 2 V. A comparison of these figures indicates that heating at 433 K produced a denser morphology. In addition, the morphology became denser after discharge–charge cycling, which may be due to long-term heating and pressing. EDS maps of the MnF_3 electrode after discharge–charge cycling are shown in Fig. S11 (ESI†). The particle size for the active manganese material is ca. 30 μm, which is much larger than that for the pristine material (ca. 1 μm, see Fig. 1). Therefore, degradation of the active electrode material is mainly caused by agglomeration during discharge–charge cycling. When the counter electrode for the

full cell is a fluoride, the manganese electrode must accept fluoride ions during the first charge process. Therefore, charge–discharge cycling was also evaluated from the fluorination of metallic Mn. The metallic manganese powder consisted of particles with two different sizes, small (<1 μm) and large (ca. 7 μm) as shown in Fig. S12 (ESI†). Fig. 4 shows discharge–charge curves for the all-solid-state fluoride battery with a metallic Mn electrode between −2 V and 2 V at 433 K. The cell had a Pb/PbF$_2$–SnF$_2$–AB/BLF/Mn–BLF–AB structure. The initial charge capacity (fluorination of the cathode) was 1087 mA h g^{-1}, which was 74% of the theoretical capacity (1463 mA h g^{-1}) for the Mn electrode. The first discharge (fluorination) capacity was 931 mA h g^{-1}, which was 63% of the theoretical capacity. This indicates slightly lower utilization efficiency compared with that starting from defluorination (75%, see Fig. 2(a)), although the difference is not significant. The open-circuit voltage before the initial charge was −0.648 V, which was higher than the theoretical potential for a MnF_2/Mn couple (−0.991 V vs. PbF$_2$/Pb). This is considered to be due to the oxidized layer formed on the metallic Mn. The second charge started from around −2 V, which indicates that the oxidized layer was removed during the initial charge and discharge process. This cell was prepared on the same day as the electrode powder. However, after the powder was stored for 11 days in a glovebox, the first defluorination capacity decreased to 690 mA h g^{-1}. This indicates that metallic manganese is highly sensitive and the oxidation layer decreases the reversible capacity. In order to compare the difference in profiles between the cases from the MnF_3 and Mn, charge–discharge profiles for all-solid-state fluoride battery with MnF_3 electrode and Mn electrode are shown in Fig. S13 (ESI†). During the initial defluorination, starting from Mn, the overall potential is high. This is influenced by the surface oxidation layer. However, from the second fluorination cycle onward, the fluorination curves show a profile similar to that of electrodes starting from MnF_3, while only the defluorination curve for the electrode starting from MnF_3 showed a short plateau for the Mn^{3+}/Mn^{2+} redox couple appeared, even though the voltage range was same. This could be due to the lower charge transfer resistance due to the high electrical conductivity of metallic Mn as a starting material. These results suggest that a manganese electrode is a promising active material for both directions, i.e., starting from defluorination or fluorination.
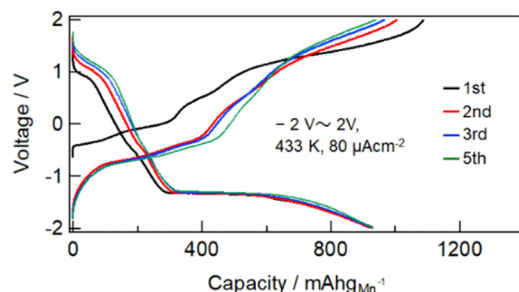

Fig. 4 Charge–discharge profiles for all-solid-state fluoride battery with metallic Mn electrode in ranges of −2 V to 2 V (starting from fluorination of metallic Mn). Cell structure is Pb/PbF$_2$–SnF$_2$–AB/BLF/Mn–BLF–AB. The capacity was calculated based on the weight of Mn.

In summary, the electrochemical reversibility of MnF_3 and metallic Mn was demonstrated in an all-solid-state fluoride battery. The MnF_3 electrode exhibited a defluorination capacity of 535 mA h g^{-1} during the initial cycle and retained a defluorination capacity of 290 mA h g^{-1} at the 50th cycle. The XAS results suggested that manganese was reduced and oxidized during the discharge–charge process. Metallic Mn was also reversibly fluorinated and defluorinated. A manganese-based electrode is thus a promising active material for fluoride batteries with a large energy storage capacity.

Data availability

The data supporting this article have been included as part of the ESI.†

Conflicts of interest

There are no conflicts to declare.

Notes and references

1 M. Zhang, X. Cao, Y. Hao, H. Wang, J. Pu, B. Chi and Z. Shen, *Energy Rev.*, 2024, **3**, 100083.
2 R. Kanno, S. Nakamura, K. Ohno and Y. Kawamoto, *Mater. Res. Bull.*, 1991, **26**, 1111–1117.
3 S. Vilminot, G. Perez, W. Granier and L. Cot, *Solid State Ionics*, 1981, **2**, 91–94.
4 Y. Ito, T. Mukoyama and S. Yoshikado, *Solid State Ionics*, 1995, **80**, 317–320.
5 L. Liu, L. Yang, M. Liu, X. Li, D. Shao, X. Luo, X. Wang and Z. Luo, *J. Alloys Compd.*, 2020, **819**, 152983.
6 F. P. Pflügl, V. Epp, S. Nakhal, M. Lerch and M. Wilkening, *Phys. Status Solidi C*, 2015, **12**, 10–14.
7 L. Xiong, P. Wen, Y. Zhang, X. Liu, J. Ning, X. Wang, H. Wang and Z. Yang, *J. Power Sources*, 2022, **518**, 230718.
8 S. Breuer and M. Wilkening, *Dalton Trans.*, 2018, **47**, 4105–4117.
9 L. Zhang, M. A. Reddy and M. Fichtner, *Solid State Ionics*, 2015, **272**, 39–44.
10 S. Breuer, S. Lunghammer, A. Kiesl and M. Wilkening, *J. Mater. Sci.*, 2018, **53**, 13669–13681.
11 J. Chable, B. Dieudonné, M. Body, C. Legein, M. P. Crosnier-Lopez, C. Galven, F. Mauvy, E. Durand, S. Fourcade, D. Sheptyakov, M. Leblanc, V. Maisonneuveb and A. Demourgues, *Dalton Trans.*, 2015, **44**, 19625–19635.
12 C. Rongeat, M. A. Reddy, R. Witter and M. Fichtner, *ACS Appl. Mater. Interfaces*, 2014, **6**, 2103–2110.
13 B. Dieudonné, J. Chable, M. Body, C. Legein, E. Durand, F. Mauvy, S. Fourcade, M. Leblanc, V. Maisonneuveb and A. Demourgues, *Dalton Trans.*, 2017, **46**, 3761–3769.
14 A. Duvel, J. Bednarcik, V. Sepelak and P. Heitjans, *J. Phys. Chem. C*, 2014, **118**, 7117–7119.
15 C. Rongeat, M. A. Reddy, R. Witter and M. Fichtner, *J. Phys. Chem. C*, 2013, **117**, 4943–4950.
16 N. Matsui, T. Seki, K. Suzuki, M. Hirayama and R. Kanno, *ACS Appl. Energy Mater.*, 2023, **6**(22), 11663–11671.
17 M. A. Reddy and M. Fichtner, *J. Mater. Chem.*, 2011, **21**, 17059–17062.
18 D. T. Thieu, M. H. Fawey, H. Bhatia, T. Diemant, V. S. Chakravadhanula, R. J. Behm, C. Kübel and M. Fichtner, *Adv. Funct. Mater.*, 2017, **27**, 1701051.
19 C. Rongeat, M. Anji Reddy, Y. Diemant, R. J. Behm and M. Fuchtner, *J. Mater. Chem. A*, 2014, **2**, 20861.
20 O. Clemens, C. Rongeat, M. A. Reddy, A. Giehr, M. Fichtner and H. Hahna, *Dalton Trans.*, 2014, **43**, 15771–115778.
21 K. Nakayama, R. Ishikawa, T. Tojigamori, H. Miki, H. Iba, N. Shibata and Y. Ikuhara, *J. Mater. Chem. A*, 2022, **10**, 3743–3749.
22 D. Zhang, K. Yamamoto, Y. Wang, S. Gao, T. Uchiyama, T. Watanabe, T. Takami, T. Matsunaga, K. Nakanishi, H. Miki, H. Iba, K. Amezawa, K. Maeda, H. Kageyama and Y. Uchimoto, *Adv. Energy Mater.*, 2021, **11**, 2102285.
23 T. Tojigamori, H. Nakajima, H. Miki, N. Matsui, T. Nakatani, S. Fujinami, K. Noi, H. Tsukasaki, K. Suzuki, M. Hirayama, S. Mori, T. Abe and R. Kanno, *ACS Appl. Energy Mater.*, 2022, **5**, 1002–1009.
24 I. Mohammad, R. Witter, M. Fichtner and M. A. Reddy, *ACS Appl. Energy Mater.*, 2018, **1**, 4766–4775.
25 K. Nakayama, H. Miki, T. Nakagawa, K. Noi, Y. Sugawara, S. Kobayashi, K. Sakurai, H. Ima, A. Kuwabara, Y. Ikuhara and T. Abe, *J. Mater. Chem. A*, 2024, **12**, 8350–8358.
26 T. Tojigamori, N. Matsui, K. Suzuki, M. Hirayama, T. Abe and R. Kannno, *ACS Appl. Energy Mater.*, 2024, **7**, 1100–1108.
27 K. Shimoda, Y. Morita, K. Noi, T. Fukunaga, Z. Ogumi and T. Abe, *ACS Energy Lett.*, 2023, **8**, 2570–2575.
28 Z. L. Cao, K. Yamamoto, T. Matsunaga, M. Kumar, N. Thakur, T. Watanabe, K. Nakanishi, H. Miki, H. Iba, K. Amezawa, H. Kageyama and Y. Uchimoto, *ACS Appl. Energy Mater.*, 2024, **7**, 6640–6648.
29 A. Inoishi, N. Setoguchi, H. Hori, E. Kobayashi, R. Sakamoto, H. Sakaebe and S. Okada, *Adv. Energy Sustainability Res.*, 2022, **3**, 2200131.
30 H. Miki, K. Yamamoto, H. Nakaki, T. Yoshinari, K. Nakanishi, S. Nakanishi, H. Iba, J. Miyawaki, Y. Harada, A. Kuwabara, Y. C. Wang, T. Watanabe, T. Matsunaga, K. Maeda, H. Kageyama and Y. Uchimoto, *J. Am. Chem. Soc.*, 2024, **146**, 3844–3853.
31 Z. L. Cao, K. Yamamoto, T. Matsunaga, T. Watanabe, M. Kumar, N. Thakur, R. Ohashi, S. Tachibana, H. Miki, K. Ide, H. Iba, H. Kiuchi, Y. Harada, Y. Orikasa and Y. Uchimoto, *Chem. Mater.*, 2024, **36**, 1928–1940.
32 S. X. Zhang, T. D. Wang, J. Zhang, Y. D. Miao, Q. Yin, Z. L. Wu, Y. J. Wu, Q. Y. Yuan and J. B. Han, *ACS Appl. Mater. Interfaces*, 2022, **14**, 24518–24525.
33 K. Rui, Z. Wen, Y. Lu, J. Jin and C. Shen, *Adv. Energy Mater.*, 2015, **5**, 1401716.
34 M. Kubin, J. Kern, M. Guo, E. Källman, R. Mitzner, V. K. Yachandra, M. Lundberg, J. Yano. and P. Wernet, *Phys. Chem. Chem. Phys.*, 2018, **20**, 16817–16827.